JOURNAL OF COMPUTATIONAL PHYSICS 107, 324–337 (1993)

Upwind Finite-Volume Method with a Triangular Mesh for Conservation Laws*

SAN-YIH LIN, TSUEN-MUH WU, AND YAN-SHIN CHIN

Institute of Aeronautics and Astronautics, National Cheng Kung University, Tainan, Taiwan, Republic of China

Received October 30, 1990; revised June 12, 1992

A new upwind scheme has been developed and analyzed for a finite-volume solution of the conservation laws on triangular meshes. The scheme is an upwind second-order extrapolation with simple local limiters, and it is weakly second-order accurate and satisfies maximum principles. In one dimension, the scheme reduces to a fully upwind second-order scheme with a simple local limiter. Preliminary numerical results demonstrating the performance of the scheme on a variety of initial-boundary value problems are presented. The order of convergence of the scheme is found to vary from 1.6 to 1.9 in L^1.

1. INTRODUCTION

The new numerical scheme is developed to compute the physically relevant solution of the initial-boundary value problem associated with the hyperbolic conservation law

$$\frac{\partial u}{\partial t}+\frac{\partial f}{\partial x}+\frac{\partial g}{\partial y}=0 \qquad \text{in} \quad \Omega\times(0,T) \qquad (1.1a)$$

$$u(x,y,0)=u_0(x,y) \qquad \text{in } \Omega \qquad (1.1b)$$

$$u(x,y,t)=r(x,y,t) \qquad \text{on} \quad \partial\Omega\times(0,T), \qquad (1.1c)$$

where $\Omega\subset R^2$, $u=(u_1,\ldots,u_m)^t$, and (f,g) is a flux such that any real combination of the Jacobian matrices $n_1(\partial f/\partial u)+n_2(\partial g/\partial u)$ has m real eigenvalues and a complete set of eigenvectors.

Theories about numerical methods solving (1.1) are far less advanced for the two-dimensional case than for the one-dimensional case. Recently, Cockburn *et al.* [4] proposed a finite-element method, RKDG, which satisfies a maximum principle for two-dimension scalar conservational laws. However, they used a stronger local limiter to enforce the maximum principle. In this paper, some simple local limiters are constructed to enforce the present finite-volume scheme to satisfy a maximum principle, thus the scheme can easily preserve high-order accuracy subject to the local limiters. The scheme developed stores the flow variables at the barycenters of the triangles. Fluid fluxes are integrated along the edges of the triangle containing the barycenter using the mid-point rule. Flow solutions are computed using TVD Runge–Kutta time integration [3, 10]. An upwind second-order extrapolation is used to evaluate the flow variables at the edges. It is interesting that the scheme reduces to a fully upwind second-order scheme with a simple local limiter in one dimension.

The objective of the present paper is to introduce and analyze a weakly second-order, upwind, finite-volume scheme. In Section 2 we present and analyze our scheme for solving scalar conservational laws. We introduce the upwind second-order extrapolation and the local limiters which do not degrade the scheme accuracy while enforcing a maximum principle. In Section 3, the present scheme is extended to solve the Euler equations. Some local limiters are introduced, based on conservative, primitive, and characteristic fields. Section 4 presents several numerical results. The numerical results of Tables I–IV indicate that the method is about $1.6\sim1.9$ order accurate in L^1. According to the paper [6], such a scheme is called weakly second-order accurate. Finally, concluding remarks are presented in Section 5.

2. GENERAL FORMULATION

2.1. *Semi-discretization Formulation*

The conservative, integral form of Eq. (1.1a) is

$$\frac{\partial}{\partial t}\iint_\Omega u\,dS+\oint_\Gamma (f,g)\cdot\mathbf{n}\,dl=0, \qquad (2.1)$$

where Ω is the domain, Γ is the boundary of Ω, and $\mathbf{n}$ is the outer unit normal. We assume the two-dimensional domain

* This paper was partially supported by the NSC, Taiwan, R.O.C.

0021-9991/93 $5.00

Ω can be discretized into a group of triangular polygons, T_h. The vertices, barycenters, and edges of the triangles K_i, are denoted by V_{ij}, C_i, and e_{ij}, $j=1, 2, 3$, respectively.

In each triangle K_i, flow variables are stored at the barycenter C_i and flow conservation is enforced on the boundary ∂K_i. If we assume that the triangular mesh is geometrically time invariant and the flow variables stored at the barycenter C_i are an area average of the integrated flow variables in the triangle K_i, then Eq. (2.1) can be written as

$$A(K_i)\frac{\partial u_i}{\partial t} = -\oint_{\partial k_i} (f, g)\cdot \mathbf{n}\, dl, \tag{2.2}$$

where $A(K_i)$ is the area of K_i.

To evaluate the right side of (2.2), we sum all the flux vectors on the three edges of K_i:

$$\oint_{\partial K_i} (f, g)\cdot \mathbf{n}\, dl = \sum_{j=1}^{3} F_{ij}\cdot |e_{ij}|, \tag{2.3}$$

where F_{ij} is the numerical approximation for the flux associated with the edge e_{ij} and $|e_{ij}|$ is the length of the edge e_{ij} (see Fig. 1).

In order to evaluate F_{ij} using an upwind scheme, it is necessary to have two fluid dynamic states, $u_{ij,L}$ and $u_{ij,R}$ (see Fig. 1). Let point M_{ij} be the midpoint of the edge e_{ij}. Given two variables $u_{ij,L}$ and $u_{ij,R}$, we can define the flux function $h_{ij}(u_{ij,L}, u_{ij,R})$ such that $h_{ij}(\cdot, \cdot)$ is any function by verifying the conditions

(1) $h_{ij}(u, u) = (f, g)\cdot \mathbf{n}_{ij}$, $h_{ji}(u, u) = (f, g)\cdot \mathbf{n}_{ji}$ (2.4a)

(2) $h_{ij}(u, v)$ is nondecreasing in u and nonincreasing in v, (2.4b)

(3) $h_{ij}(\cdot, \cdot)$ is Lipschitz, (2.4c)

(4) $h_{ij}(u_L, u_R) = -h_{ji}(u_R, u_L)$, (2.4d)

where $\mathbf{n}_{ij}$ is the outer unit normal of the edge and e_{ij} corresponding to the triangle K_i such that $\mathbf{n}_{ij} = -\mathbf{n}_{ji}$. Examples of h can be found in [3, 5]. In this way, Eq. (2.2) become

$$A(K_i)\frac{du_i}{dt} = -\sum_{j=1}^{3} h_{ij}(u_{ij,L}, u_{ij,R})\cdot |e_{ij}| \qquad \text{for all } i. \tag{2.5}$$

Now, we introduce a second order extrapolation to evaluate the left and right Riemann states for the upwind solver. Referring to Fig. 2, we use the three variables u_0, u_2, u_3 corresponding to barycenters C_0, C_2, C_3 to extrapolate the left variables $u_{01,L}$. Since the values of three points determine a linear function in a two-dimensional space, the linear function is given by

$$u \sim (u_2 - u_0)\lambda_2 + (u_3 - u_0)\lambda_3 + u_0, \tag{2.6}$$

where λ_j is the barycentric coordinates such that $\lambda_j(C_k) = \delta_{jk}$, $j, k = 0, 2, 3$.

Therefore, the variable $u_{01,L}$ is expressed by

$$u_{01,L} = (u_2 - u_0)\lambda_2(M_1) + (u_3 - u_0)\lambda_3(M_1) + u_0. \tag{2.7}$$

Similarly, we can evaluate the right Riemann state $u_{01,R}$. The signs of $\lambda_j(M_1)$ are nonpositive for most of triangulations.

2.2. *The Maximum Principle, the Local Limiter and TVD Triangulations*

From Section 2.1, we can see that the scheme can be expressed in the form

$$\frac{du_i}{dt} = \sum_{j=1}^{3} c_{ij}(u_{ij} - u_i), \tag{2.8}$$

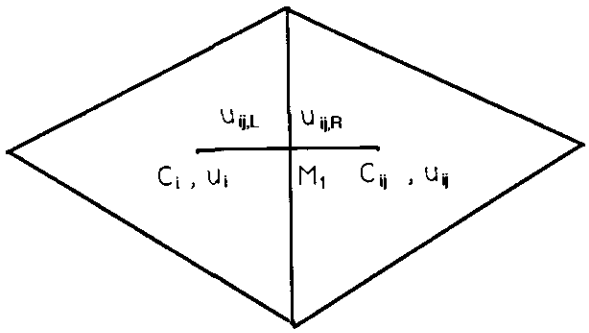

FIG. 1. Representative variables of two fluid dynamics states $u_{ij,L}$ and $u_{ij,R}$.

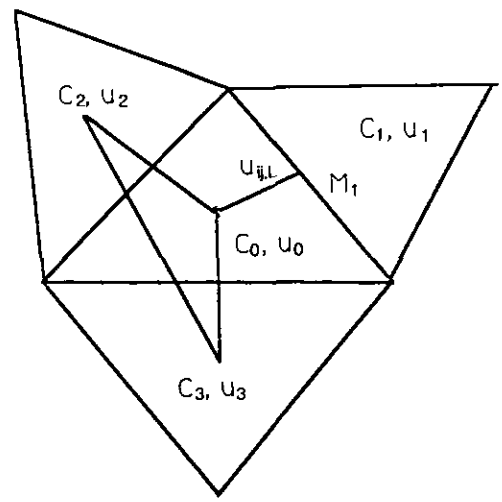

FIG. 2. Representative variable $u_{01,L}$ at point M_1.

where u_{ij} are the variables of barycenters c_{ij} of the triangle K_{ij} with $K_{ij} \cap K_i = e_{ij}$. Then we require all the coefficients to be nonnegative [7]:

$$c_{ij} \geqslant 0, \qquad j = 1, 2, 3. \tag{2.9}$$

This condition on the signs of the coefficients, which is a direct generalization of the condition for a one-dimensional three-point scheme to be TVD, assures that a maximum cannot increase. The rest of this section is to introduce the local limiters that are enforced to satisfy condition (2.9). The idea of the following analysis is similar to sections 2.3 and 2.4 in Ref. [4].

From the definition of the flux h, we have

$$\sum_{j=1}^{3} h_{ij}(u_i, u_i) \cdot |e_{ij}| = 0 \qquad \text{for al } i. \tag{2.10}$$

Rewrite the right-hand side of (2.5) as

$$\begin{aligned}
&-\sum_{j=1}^{3} h_{ij}(u_{ij,L}, u_{ij,R}) \cdot |e_{ij}| \\
&\quad = -\sum_{j=1}^{3} [h_{ij}(u_{ij,L}, u_{ij,R}) - h_{ij}(u_i, u_i)] \cdot |e_{ij}| \\
&\quad = -\sum_{j=1}^{3} \{|h_{ij}(u_{ij,L}, u_{ij,R}) - h_{ij}(u_i, u_{ij,R})] \cdot |e_{ij}| \\
&\qquad + [h_{ij}(u_i, u_{ij,R}) - h_{ij}(u_i, u_i)] \cdot |e_{ij}|\} \\
&\quad = \sum_{j=1}^{3} -|e_{ij}| \cdot h_{ij,1} \cdot (u_{ij,L} - u_i) \\
&\qquad + \sum_{j=1}^{3} -|e_{ij}| \cdot h_{ij,2} \cdot (u_{ij,R} - u_i) \\
&\quad = \sum_{j=1}^{3} -|e_{ij}| \cdot h_{ij,1} \cdot (u_{ij,L} - u_i) \\
&\qquad + \sum_{j=1}^{3} -|e_{ij}| \cdot h_{ij,2} \cdot [(u_{ij,R} - u_{ij}) + (u_{ij} - u_i)],
\end{aligned} \tag{2.11}$$

where $h_{ij,1}$ is the u-derivative of h_{ij} evaluated at some points and $h_{ij,2}$ is the v-derivative of h_{ij} evaluated at some points. From (2.4b) we have $h_{ij,1} \geqslant 0$ and $h_{ij,2} \leqslant 0$. Now, we first study the first term in RHS of Eq. (2.11). For fixed $j = 1$, we have

$$\begin{aligned}
&-|e_{i1}| \cdot h_{j1,1} \cdot (u_{i1,L} - u_i) \\
&\quad = -|e_{i1}| \cdot h_{i1,1}[(u_{i2} - u_i)\, \lambda_{i2}(M_{i1}) \\
&\qquad + (u_{i3} - u_i)\, \lambda_{i3}(M_{i1})] \\
&\quad -|e_{i1}| \cdot h_{i1,1} \cdot \lambda_{i2}(M_{i1}) \cdot (u_{i2} - u_i) - |e_{i1}| \\
&\qquad \cdot h_{i1,1} \cdot \lambda_{i3}(M_{i1}) \cdot (u_{i3} - u_i).
\end{aligned} \tag{2.12}$$

Then the first condition to achieve the maximum principle is

$$\lambda_{ij}(M_{ik}) \leqslant 0, \qquad j, k = 1, 2, 3, \quad j \neq k \qquad \text{for all } i \tag{2.13}$$

For the second term in RHS of Eq. (2.11), by following the theorem in [8], we need to require that

$$0 \leqslant \frac{u_{ij,R} - u_{ij}}{u_i - u_{ij}} \leqslant 1 \tag{2.14}$$

From Eq. (2.13), we have to restrict ourselves to consider a special class of triangulation T_h.

DEFINITION 2.1. A triangulation T_h is said to be TVD-triangulation, if for each triangle K_i, the condition (2.13) is satisfied.

From the condition (2.14), we define the local limiter P_{ij}^1 as

$$P_{ij}^1 : R \to R \tag{2.15a}$$

such that

$$\begin{aligned}
u_{ij,L}^{\text{new}} &\equiv P_{ij}^1(u_{ij,L}) \\
&= \text{minmod}(u_{ij,L} - u_i, k \cdot (u_{ij} - u_i)) + u_i,
\end{aligned} \tag{2.15b}$$

where k is some positive constant such that $k \geqslant 0.5$, and minmod is the function:

$$\text{minmod}(a, b) = \begin{cases} \min(|a|, |b|) \cdot \text{sign } a & \text{if sign } a = \text{sign } b \\ 0 & \text{otherwise.} \end{cases}$$

Now, by applying the local limiter (2.15), Eq. (2.11) becomes

$$\begin{aligned}
&-\sum_{j=1}^{3} h_{ij}(u_{ij,L}^{\text{new}}, u_{ij,R}^{\text{new}}) \cdot |e_{ij}| \\
&\quad = \sum_{j=1}^{3} -|e_{ij}| \cdot h_{ij,1}(u_{ij,L}^{\text{new}} - u_i) \\
&\qquad + \sum_{j=1}^{3} -|e_{ij}| \cdot h_{ij,2}[(u_{ij,k}^{\text{new}} - u_{ij}) + (u_{ij} - u_i)]
\end{aligned} \tag{2.16a}$$

where

$$\begin{aligned}
u_{i1,L}^{\text{new}} - u_i &= c \cdot (u_{i1,L} - u_i) \\
&= c \cdot [(u_{i2} - u_i) \cdot \lambda_{i2} \cdot (M_{i1}) \\
&\qquad (u_{i3} - u_i) \cdot \lambda_{i3} \cdot (M_{i1})].
\end{aligned} \tag{2.16b}$$

By Eq. (2.15b), we have that $0 \leqslant c \leqslant 1$. Therefore, combining Definition 2.1 and the local limiter P_{ij}^1, we have proven the following result:

THEOREM 2.2. *Let P_{ij}^1 be the limiter defined by* (2.15) *and let T_h be TVD-triangulation, then the scheme* (2.8) *satisfies the maximum principle, i.e., the coefficients C_{ij}'s of Eq.* (2.8) *satisfy Eq.* (2.9).

Remark 2.3. For some TVD triangulations, the scheme with the limiter P_{ij}^1 will lose second-order accuracy. Here, we introduce two other limiters. First, from the second term in the RHS of Eq. (2.11), if the quantity $u_{ij,L}-u_i$ can be written as a positive linear combination of $u_{ik}-u_i$, $k=1, 2, 3$, the scheme (2.5) still satisfies the maximum principle. Observing Fig. 3, the vector $\mathbf{C}_i\mathbf{M}_1$ can be expressed as a positive linear combination of vectors $\mathbf{C}_i\mathbf{C}_{i1}$ and $\mathbf{C}_i\mathbf{C}_{i2}$, as

$$\mathbf{C}_i\mathbf{M}_1=\theta_1\mathbf{C}_i\mathbf{C}_{i1}+\theta_2\mathbf{C}_i\mathbf{C}_{i2},$$

where $\theta_1, \theta_2 \geqslant 0$. Define

$$U_{i1}=\theta_1\cdot(u_{i1}-u_i)+\theta_2\cdot(u_{i2}-u_i)$$

and the second limiter P_{i1}^2 as

$$P_{i1}^2: R\to R,$$

such that

$$u_{i1,L}^{\text{new}}\equiv P_{i1}^2(u_{i1,L})=\text{minmod}(u_{i1,L}-u_i, k'\cdot U_{i1})+u_i, \quad (2.17)$$

where $k'\geqslant 1$. One can see that this local limiter will preserve second-order accuracy for smooth solutions.

Second, we modify the idea of Barth's limiter [1] and define

$$u_i^{\max}=\max(u_i, u_{i1}, u_{i2}, u_{i3}), \quad u_i^{\min}=\min(u_i, u_{i1}, u_{i2}, u_{i3})$$

and, if $u_{i1,L}-u_i>0$, then

$$u_{i1,L}^{\text{new}}\equiv P_{i1}^3(u_{i1,L})$$
$$=\text{minmod}(u_{i1,L}-u_i, k\cdot(u_i^{\max}-u_i)+M\cdot h^2)+u_i;$$

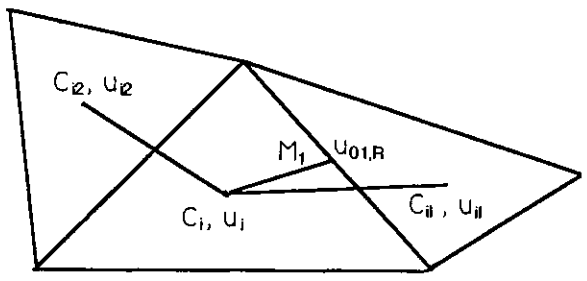

FIG. 3. Vector $\mathbf{C}_i\mathbf{M}_1$ can be expressed as positive linear combination of vectors $\mathbf{C}_i\mathbf{C}_{i1}$ and $\mathbf{C}_i\mathbf{C}_{i2}$.

if $u_{i1,L}-u_i=0$, then

$$u_{i1,L}^{\text{new}}\equiv P_{i1}^3(u_{i1,L})=u_i;$$

if $u_{i1,L}-u_i<0$, then

$$u_{i1,L}^{\text{new}}\equiv P_{i1}^3(u_{i1,L})$$
$$=\text{minmod}(u_{i1,L}-u_i, k\cdot(u_i^{\min}-u_i)-M\cdot h^2)+u_i, \quad (2.18)$$

where $k\geqslant 0.5$, $M\geqslant 0$, and h is the smallest length of edges. This limiter is the weakest one which can preserve order accuracy, but it may not satisfy the maximum principle even for $M=0$. The choice of M is state of the art; one can refer to [3, 4].

Remark 2.4. We note that the scheme with the local limiters P_{ij}^1 and P_{ij}^2 reduces to the following fully upwind second-order scheme with a simple local limiter in one dimension:

$$\begin{aligned} u_{j+1/2,R}&=u_{j+1}-\tfrac{1}{2}\cdot(u_{j+2}-u_{j+1})\\ u_{j+1/2,L}&=u_j+\tfrac{1}{2}\cdot(u_j-u_{j-1}). \end{aligned} \quad (2.19)$$

Here, let u_j be the numerical approximation at $x=j\,\Delta x$ and the local limiter is defined by

$$u_{j+1/2,L}^{\text{new}}=\text{minmod}(u_{j+1/2,L}-u_i, k\cdot(u_{j+1}-u_i))+u_i. \quad (2.20)$$

2.3. *TVD Runge–Kutta Time Integration*

A second-order TVD Runge–Kutta time integration scheme [3, 10] was used to integrate the ODE (2.5). Runge–Kutta time integration is an explicit scheme which is easy to evaluate and simple to implement.

Define a residual as

$$R_i(u)=\frac{-1}{A(K_i)}\sum_{j=1}^{3}h_{ij}(u_{ij,L}, u_{ij,R})\cdot|e_{ij}| \qquad \text{for all } i. \quad (2.21)$$

The second-order TVD Runge–Kutta time stepping scheme is then:

$$\begin{aligned} u_i^{(0)}&=u_i^n\\ u_i^{(1)}&=u_i^{(0)}+\Delta t\,R_i(u^{(0)})\\ u_i^{(2)}&=u_i^{(1)}+\Delta t\,R_i(u^{(1)})\\ u_i^{n+1}&=0.5(u_i^{(0)}+u_i^{(2)}). \end{aligned} \quad (2.22)$$

Define

$$\mathrm{CFL} = \sup_{e \in \partial K, K \in T_h} \Delta t \frac{|e|}{|K|} \|h' \cdot n_{e,K}\|_{L^\infty[a_0, b_0]} \tag{2.23a}$$

$$a_0 = \inf\{\inf_{(x,y)\in\Omega} u_0(x, y), \inf_{(x,y)\in\partial\Omega} r(x, y, t)\} \tag{2.23b}$$

$$b_0 = \sup\{\sup_{(x,y,\Omega)} u_0(x, y), \sup_{(x,y)\in\partial\Omega} r(x, y, t)\}. \tag{2.23c}$$

It is not difficult to see that the fully discretized scheme (2.22) with $\mathrm{CFL} \leqslant 1/(6+3k)$ satisfies the maximum principle.

3. EULER EQUATIONS

3.1. *Governing Equation*

The flows of two-dimensional, compressible, inviscid fluid, can be described in conservation form by the Euler equations,

$$w_t + f_x + g_y = 0, \tag{3.1}$$

where

$$w = \begin{pmatrix} \rho \\ \rho u \\ \rho v \\ \rho e \end{pmatrix}, \quad f = \begin{pmatrix} \rho u \\ \rho u^2 + p \\ \rho uv \\ u(\rho e + p) \end{pmatrix}, \quad g = \begin{pmatrix} \rho v \\ \rho uv \\ \rho v^2 + p \\ v(\rho e + p) \end{pmatrix},$$

here p, ρ, (u, v), and ρe are the pressure, density, the Cartesian velocity components, and the total energy per unit volume, respectively.

The system of equations is closed by the equation of state for a perfect gas,

$$p = (\gamma - 1)(\rho e - \tfrac{1}{2}\rho(u^2 + v^2)),$$

where γ is the ratio of specific heats and typically taken as 1.4 for air.

3.2. *Local Limiter*

The extension of the method to solve Euler equations is straightforward except for the choice of local limiters. Usually, one can choose a conservative, primitive, or characteristic field as a basis to define a local limiter, since a local limit defined by conservative or primitive fields is easily constructed. Here, we only introduce the characteristic-field limiter.

Let

$$J_{ij} = \left(\frac{\partial f}{\partial w}\mathbf{n}_{ij,x} + \frac{\partial g}{\partial w}\mathbf{n}_{ij,y}\right)\Big|_{w=w^*}, \tag{3.2}$$

which is the jacobian matrix. Here $(\mathbf{n}_{ij,x}, \mathbf{n}_{ij,y}) = \mathbf{n}_{ij}$ and w^* is equal to w_i or $\frac{1}{2}(w_i + w_{ij})$. Denote the eigenvalues, the left and right eigenvectors of J_{ij} by $\lambda_{ij}^{(p)}$, $l_{ij}^{(p)}$, and $r_{ij}^{(p)}$, $p = 1, \ldots, 4$. Normalize the left and right eigenvectors as

$$l_{ij}^{(p)} \cdot r_{ij}^{(q)} = \delta_{pq}$$

and project every vector to the eigenspace J_{ij},

$$a^{(p)} = l_{ij}^{(p)} \times a,$$

where a is $w_{ij,L} - w_i$ or $w_{ij} - w_i$.

Apply the local limiter, P_{ij}^1, to each characteristic field

$$(w_{ij,L} - w_i)^{(p)(\mathrm{mod})} = \mathrm{minmod}((w_{ij,L} - w_i)^{(p)}, k \cdot (w_{ij} - w_i)^{(p)}).$$

Finally, transform $(w_{ij,L} - w_i)^{(p)(\mathrm{mod})}$ back by means of the relation

$$(w_{ij,L} - w_i)^{(\mathrm{mod})} = \sum_{p=1}^{4} (w_{ij,L} - w_i)^{(p)(\mathrm{mod})}.$$

Therefore, we obtain

$$w_{ij,L}^{\mathrm{new}} = (w_{ij,L} - w_i)^{(\mathrm{mod})} + w_i. \tag{3.3}$$

Although it is more complicated to compute, it has more physical senses for the Euler equations [3, 9].

4. EXAMPLES FOR NUMERICAL RESULTS

4.1. *Scalar Conservational Laws*

In this subsection, three examples are used to test the ability of capturing discontinuity and the order of accuracy

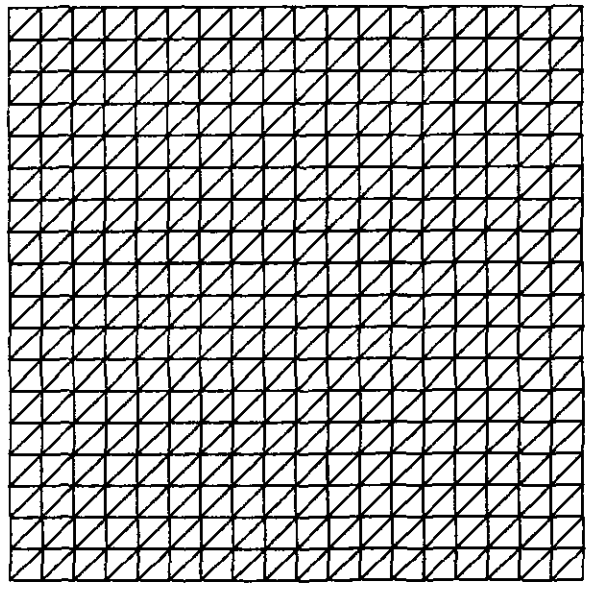

FIG. 4. The triangulation: $20 \times 20 \times 2$ triangles.

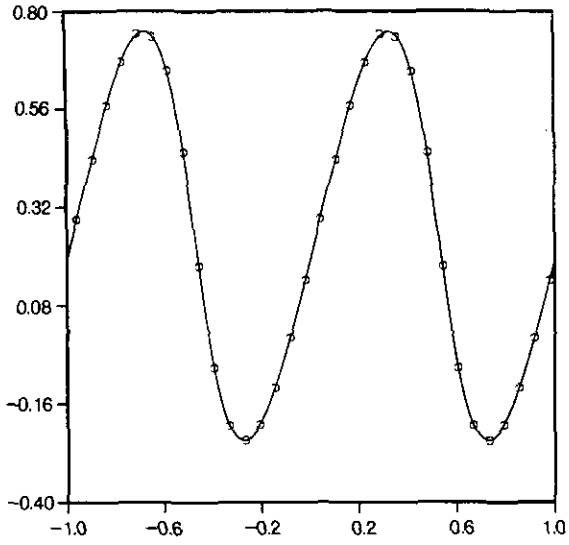

FIG. 5. Examples 3.1 with Lax–Friedrichs flux, $T=0.1$, CFL $=0.4$, $32\times32\times2$ triangles. The solution cut along the diagonal.

of our scheme. We use Lax–Friedrichs monotone and Godunov flux to compute the flux, h_{ij}, and compare the differences between them. The grid system whose element numbers are $M\times N\times2$ is shown in Fig. 4. It is easy to check that this triangulation is TVD-triangulation. The local limiter, P_{ij}^1, is used in those tests. On the used triangulations, the projection still preserve the potential second-order accuracy of the method and the two local limiters P_{ij}^1 and P_{ij}^2, are equal to each other. Note that the L^∞-error is evaluated at the barycenter and the L^1-error is obtained by multiplying that value by the area of the triangle.

EXAMPLE 1. In this problem, we consider the Burgers equation with periodic boundary conditions,

$$u_t+\left(\frac{u^2}{2}\right)_x+\left(\frac{u^2}{2}\right)_y=0, \qquad \text{in} \quad (0,T)\times\Omega, \quad (4.1a)$$

$$u(t=0,x,y)=\frac{1}{4}+\frac{1}{2}\sin(\pi(x+y)), \qquad (x,y)\in\Omega, \quad (4.1b)$$

where the domain Ω is the square $(-1,1)\times(-1,1)$.

At $T=0.1$ the solution is smooth. Figure 5 shows the curve cut along the diagonal computed by means of the Lax–Friedrichs flux. The L^1, L^∞ errors and the orders of accuracy of the solution are displayed on Tables I and II for the schemes with Lax–Friedrichs and Godunov flux, respectively.

TABLE I

Smooth Solution for $T=0.1$ with Lax–Friedrichs Flux

M	L_1 error	Order	L_∞ error	Order
8	4.331E−02		3.155E−02	
16	1.340E−02	1.63	1.133E−02	1.48
32	4.138E−03	1.76	4.263E−03	1.41
64	1.238E−03	1.74	1.973E−03	1.11

TABLE II

Smooth Solution for $T=0.1$ with Godunov Flux

M	L_1 error	Order	L_∞ error	Order
8	4.495E−02		3.395E−02	
16	1.410E−02	1.67	1.133E−02	1.58
32	4.161E−03	1.76	4.262E−03	1.41
64	1.234E−03	1.75	1.981E−04	1.21

At $T=0.5$, solution presents a discontinuous curve (see Fig. 6), which is cut along the diagonal, computing by means of the Lax–Friedrichs flux. We can see how the discontinuity has been captured by one cell. Similarily, L^1, L^∞ errors and orders are displayed in Tables III and IV for the two fluxes. When the solution is smooth, the performances of Lax–Friedrichs and Godunov fluxes are almost equal.

EXAMPLE 2. We consider the initial-boundary value problem of the Burgers equation:

$$u_t+\left(\frac{u^2}{2}\right)_x+\left(\frac{u^2}{2}\right)_y=0, \qquad \text{in} \quad (0,T)\times\Omega, \quad (4.2a)$$

$$u(t=0,x,y)=\begin{cases}-0.2, & \text{for} \quad x>0,\ y>0\\ -1.0, & \text{for} \quad x<0,\ y>0\\ 0.5, & \text{for} \quad x<0,\ y<0,\ (x,y)\in\Omega\\ 0.8, & \text{for} \quad x>0,\ y<0,\end{cases} \quad (4.2b)$$

$$u(t,x,y)=v(t,x,y), \qquad (x,y)\in\partial\Omega, \quad (4.2c)$$

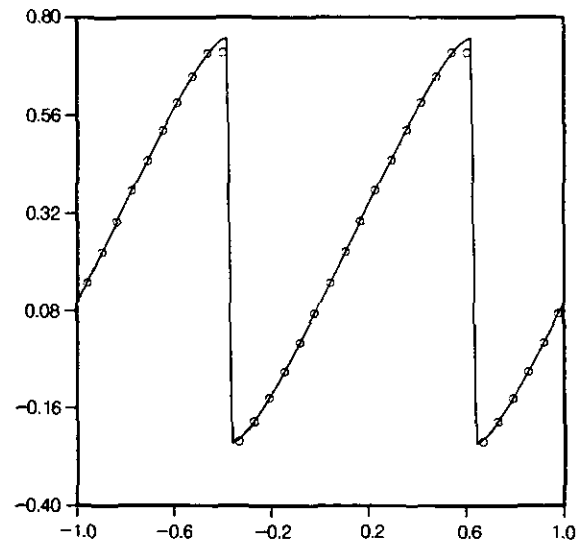

FIG. 6. Example 3.1 with Lax–Friedrichs flux, $T=0.5$, CFL $=0.4$, $32\times32\times2$ triangles. The solution cut along the diagonal.

TABLE III

Discontinuity Solution for $T=0.5$ and Lax–Friedrichs Flux

M	L_1 error	Order	L_∞ error	Order
8	1.426E−03		7.548E−03	
16	6.436E−04	1.15	2.531E−03	1.58
32	1.837E−04	1.81	1.477E−03	0.78
64	5.212E−05	1.82	6.391E−04	1.21

Note. Computing domain: $[-0.25, 0.5]\times[-.25\times 0.5]$.

where v is the exact solution of problem (4.2) and Ω is the square $[-1, 1]\times[-1, 1]$. In Figs. 7 and 9, we show the level curves of the approximate solution and curve cut along $y=-\frac{1}{96}$ at $T=1.0$ with Lax–Friedrichs flux. Similarily, Figs. 8 and 10 show the contour and curve by means of Godunov flux. In this example, the grid system is constructed by $64\times 64\times 2$ triangle meshes. From Figs. 9 and 10, we can see that Godunov method presents slightly better solutions than Lax–Friedrichs does.

EXAMPLE 3. The last problem we consider is a two-dimensional boundary layer problem:

$$u_t+\left(\frac{u^2}{2}\right)_x+u_y=0, \qquad 0\leqslant x\leqslant 1, \quad 0\leqslant y\leqslant 1 \tag{4.3a}$$

$$u(x, 0, t)=a+b\sin(2\pi x), \tag{4.3b}$$

$$u \text{ is periodic in } x \text{ with period } 1. \tag{4.3c}$$

The initial condition is $u(x, y, 0)=a+b\sin(2\pi x)$. Enforce (4.3b) at $y=0$ and solve the problem to steady state with the criterion $\|u^{n+1}-u^n\|_{L^1}<10^{-7}$. Figures 11 and 12 show the contours for $a=0.5$, $b=1$, and $a=0$, $b=1$, respectively. Lax–Friedrichs flux with $32\times 32\times 2$ triangular meshes is used in this example. One point we need to mention is that, in Fig. 12, the second case, $a=0$ and $b=1$, shows a more smearing solution at the right-hand side of the shock. We suspect that this phenomenon was produced by the grid orientation around the shock. In the next section, one can see the effect of grid orientations for the Euler equations.

TABLE IV

Discontinuity Solution for $T=0.5$ with Godunov Flux

M	L_1 error	Order	L_∞ error	Order
8	1.505E−03		7.968E−03	
16	6.596E−04	1.20	2.531E−03	1.65
32	1.861E−04	1.83	1.631E−03	0.63
64	5.297E−05	1.81	7.179E−04	1.18

Note. Computing domain: $[-0.25, 0.5]\times[-0.25, 0.5]$.

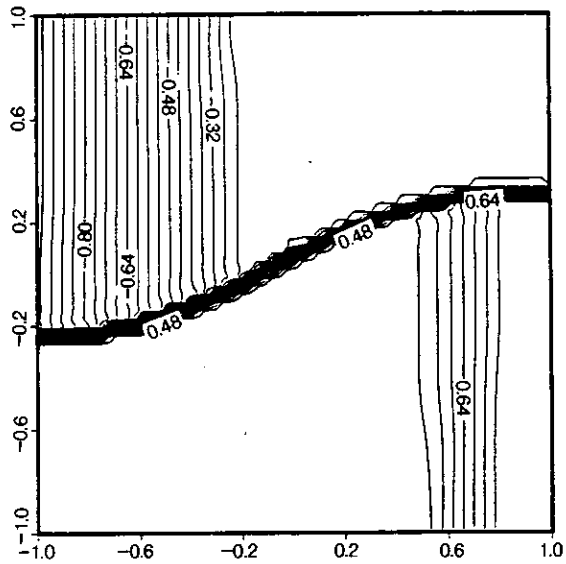

FIG. 7. Example 3.2 with Lax–Friedrichs flux, $T=1.0$, CFL $=0.4$, $64\times 64\times 2$ triangles. The level curves.

4.2. *Example for Euler Equations*

In this subsection, two examples are tested for the Euler equations. In Example 4, we will study three subjects: grid orientations, the vector fields for the basis of local limiters, and the choice of k in Eq. (2.15b). In Example 5, we will study the local limiter, P_{ij}^3, in detail.

EXAMPLE 4. The oblique shock reflection [11]. We solve a steady flow problem that is an oblique shock wave impinging to a solid surface with an incident shock wave angle of 29.88° and inflow Mach number 2.9. The computa-

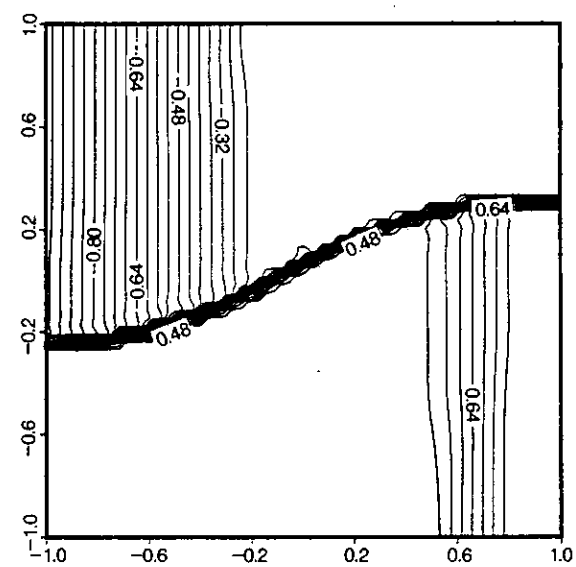

FIG. 8. Example 3.2 with Godunov flux, $T=1.0$, CFL $=0.4$, $64\times 64\times 2$ triangles. The level curves.

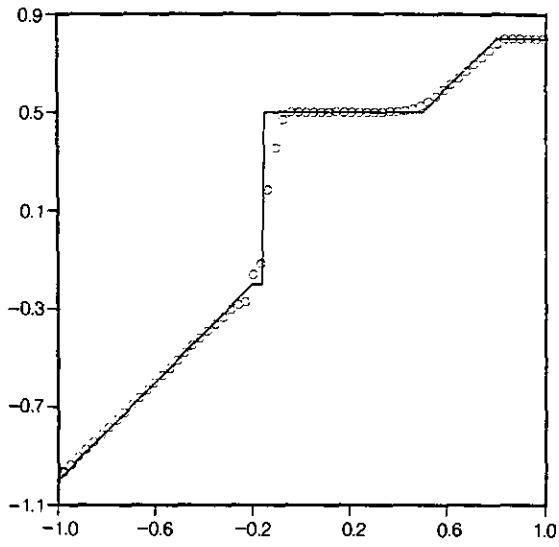

FIG. 9. Example 3.2 with Lax–Friedrichs flux. The solutions cut along $y = \frac{1}{96}$.

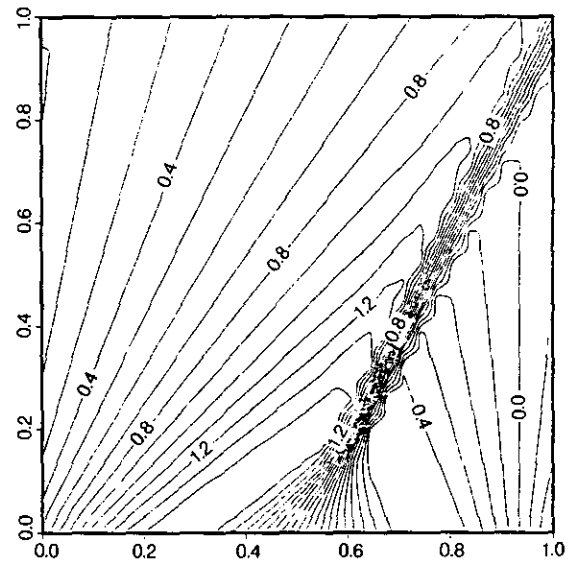

FIG. 11. Example 3.3 with $a = 0.5$, $b = 1.0$ with Lax–Friedrichs flux, $32 \times 32 \times 2$ triangles. The level curves.

tional domain Ω is $(0, 4) \times (0, 1)$. First, choose $k = 1$ and the grid system to be $80 \times 20 \times 4$. We test our scheme with four different vector fields: the conservative, primitive, and two characteristic fields for the basis of local limiters. We call the scheme with characteristic-field limiter and $w^* = \frac{1}{2}(w_i + w_{ij})$ in Eq. (3.2) as characteristic I, and the scheme with a characteristic-field limit and $w^* = w_i$ as characteristic II. From Fig. 13, the numerical results indicate that the performance of characteristics I and II are better and almost equally better. Second, we study the method, characteristic I, with a grid system of $80 \times 20 \times 4$ and different k's, $k = 1.0$, 0.95, 0.9, and 0.8. In a theoretical point of view [7], if k is larger than 0.5, the method with local limiters preserves second-order accuracy for a uniform grid system. From Figs. 14a and 14b, one can see that their performance is almost equally better. However, the convergence history, as shown in Fig. 15, indicates that a scheme with smaller k can achieve a better convergence rate. It is surprising that a scheme with the conservation-field limiter and $k = 0.8$ can also achieve a higher order accuracy and a free-oscillation solution as the schemes characteristics I and II do. This indicates that our scheme can perform very well without using any characteristic-field decompositions. Finally, we

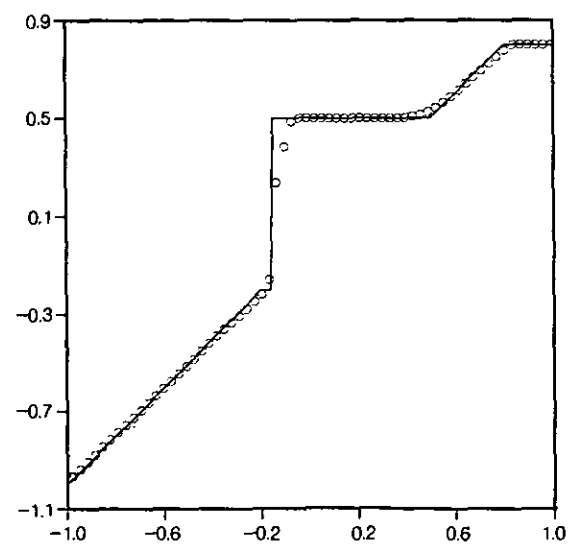

FIG. 10. Example 3.2 with Godunov flux. The solution cut along $y = \frac{1}{96}$.

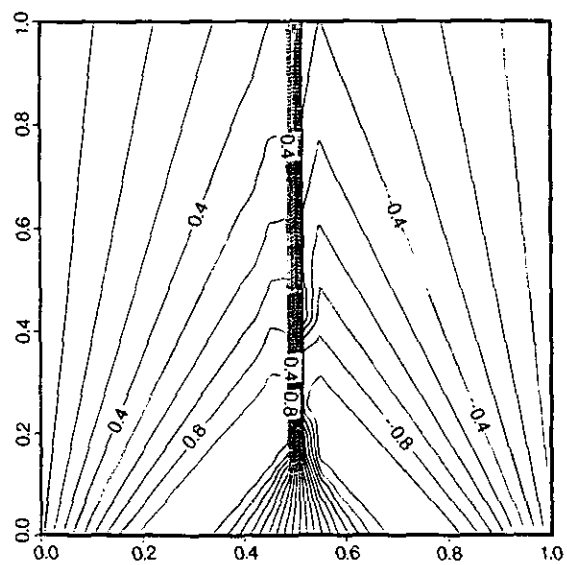

FIG. 12. Example 3.3 with $a = 0$, $b = 1.0$ with Lax–Friedrichs flux, $32 \times 32 \times 2$ triangles. The level curves.

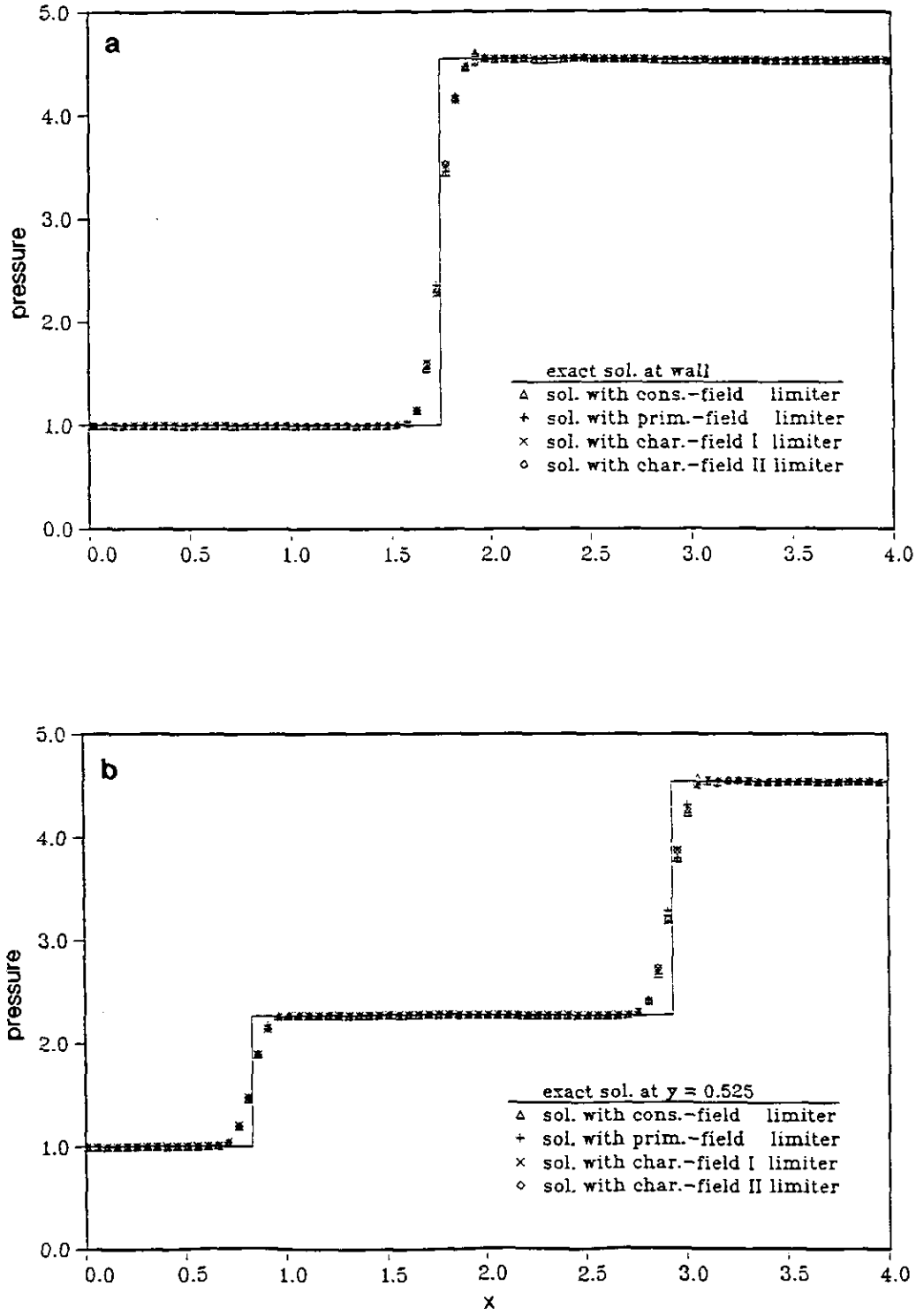

FIG. 13. (a) Pressure distribution at wall. (b) Pressure distribution at $y = 0.525$ for the oblique shock reflection problem.

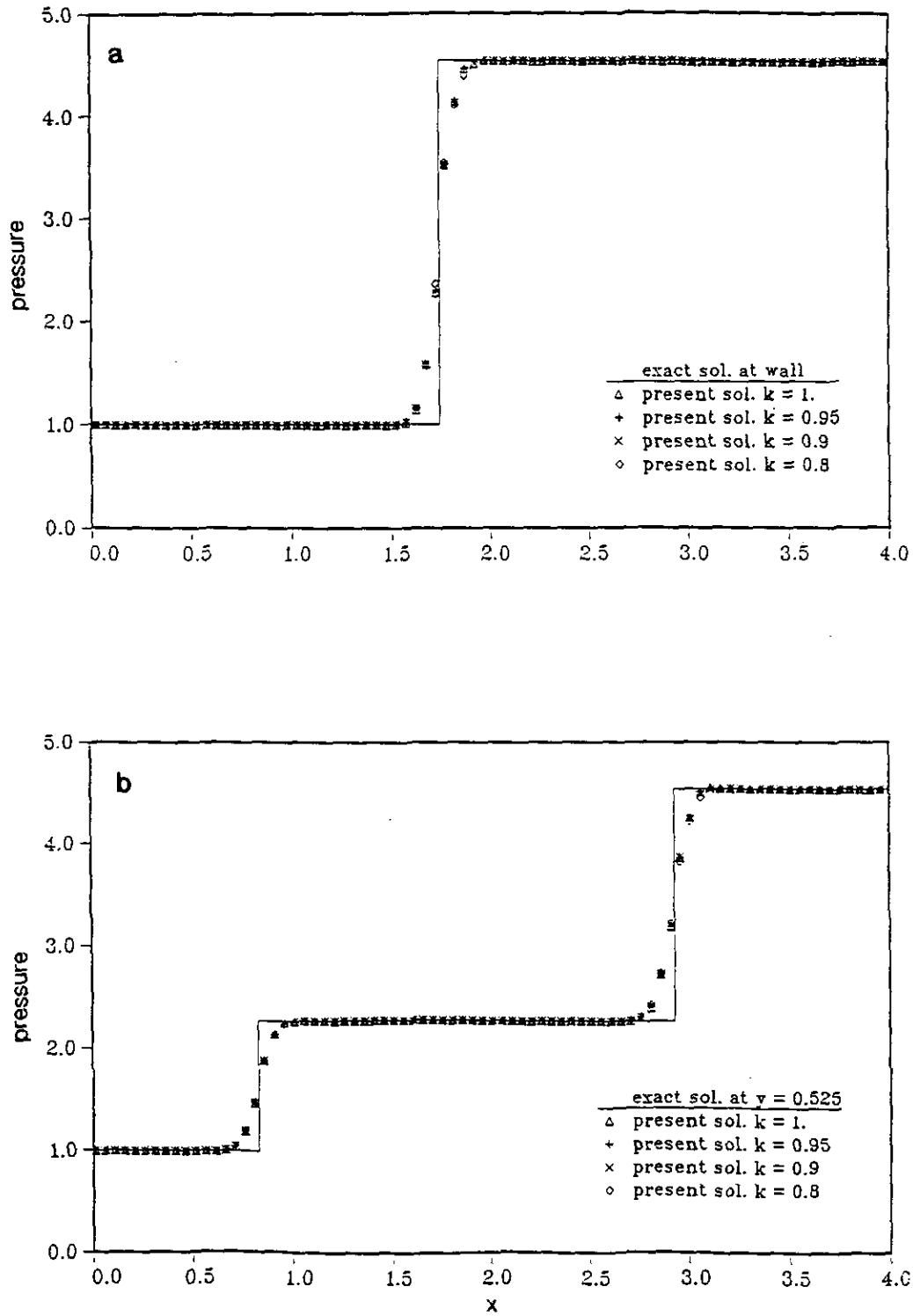

FIG. 14. (a) Pressure distribution at wall. (b) Pressure distribution at $y = 0.525$ for the oblique shock reflection problem.

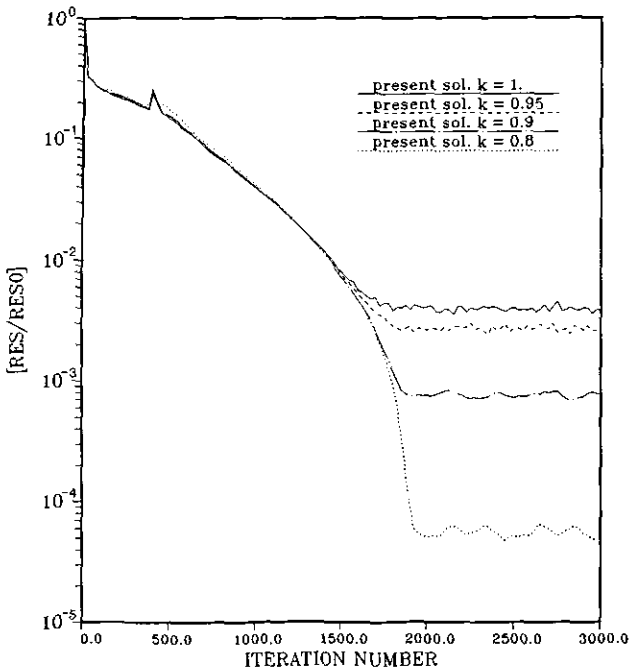

FIG. 15. Convergence history for the oblique shock reflection problem.

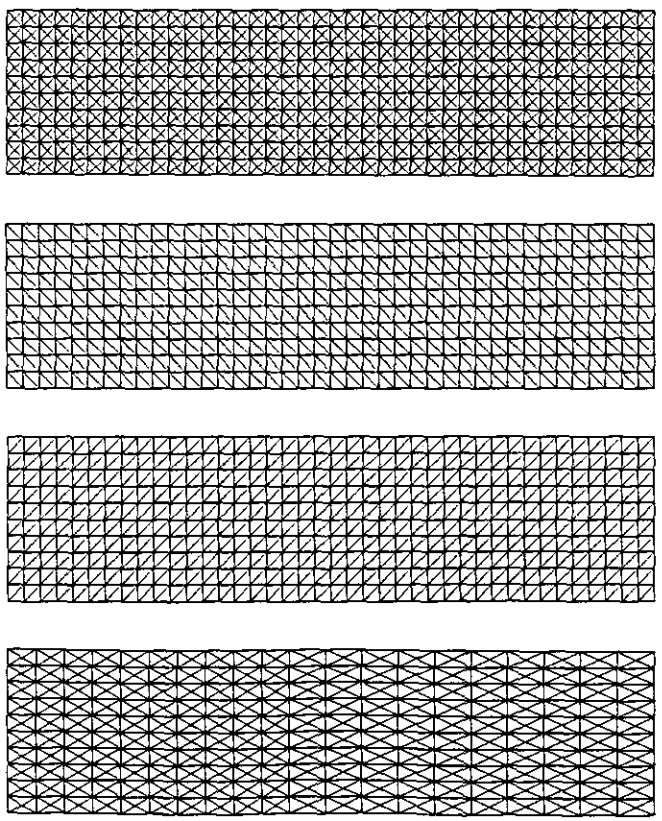

FIG. 16. The grid systems for the oblique shock reflection problem.

TABLE V

Errors and Order Accuracy of Density for Ringleb's Problem

$M \times N \times 4$	L_1 error	Order	L_∞ error	Order
$8 \times 2 \times 4$	8.222E − 03		4.093E − 02	
$16 \times 4 \times 4$	1.706E − 03	2.27	1.305E − 02	1.65
$24 \times 6 \times 4$	7.200E − 04	2.13	6.513E − 03	1.71
$32 \times 8 \times 4$	1.884E − 04	4.66	2.475E − 03	3.36

Note. Using the scheme with no limiter.

study the method, characteristic I with $k = 1$ and four different grid systems, $80 \times 20 \times 4$, $80 \times 20 \times 2r$, $80 \times 20 \times 2l$, $40 \times 20 \times 4$ (see Fig. 16). On the grid system $80 \times 20 \times 2r$, from Figs. 17a and 17b, the scheme can capture the incident shock much better than the reflected one. On the other hand, on the grid system $80 \times 20 \times 2l$, the effect is changed. The overall conclusion is that the performance of the scheme is very sensitive to the grid orientation, when triangles are aligned with the shock, the scheme can perform well on a coarse grid.

EXAMPLE 5. The Ringleb's problem [2]. For the Ringleb's problem, there exists a smooth exact solution which is supersonic at inflow and subsonic at outflow. The grid system used is $32 \times 8 \times 4$, as shown in Fig. 18. From Fig. 19a, near the turning point O, the gradient of the solution is very large. We test the schemes by the local limiter, P_{ij}^3, with conservation-field bases and $M = 0$, 10, and ∞. The last one is equal to the scheme with no limiter which is a pure upwind scheme. From Tables V and VI and Figs. 19b, 19c, one can see that the last two schemes preform very well. Comparing Tables VI and VII, much improvement is gained for $M = 10$. From our experience, this example is a good test problem to see the difference between TVD and TVB schemes for the two-dimensional Euler equations.

5. CONCLUSION

A numerical scheme has been developed and analyzed for the finite-volume solution of two-dimensional conservation laws on triangular meshes. The scheme satisfies the maximum principle for general nonlinear fluxes if the triangulations are TVD triangulations. We have investigated and

TABLE VI

Errors and Order Accuracy of Density for Ringleb's Problem

$M \times N \times 4$	L_1 error	Order	L_∞ error	Order
$8 \times 2 \times 4$	8.221E − 03		4.093E − 02	
$16 \times 4 \times 4$	1.705E − 03	2.27	1.305E − 02	1.65
$24 \times 6 \times 4$	7.192E − 04	2.13	6.513E − 03	1.71
$32 \times 8 \times 4$	1.880E − 04	4.66	2.474E − 03	3.37

Note. Using the scheme with P_{ij}^3 limiter and $M = 10$.

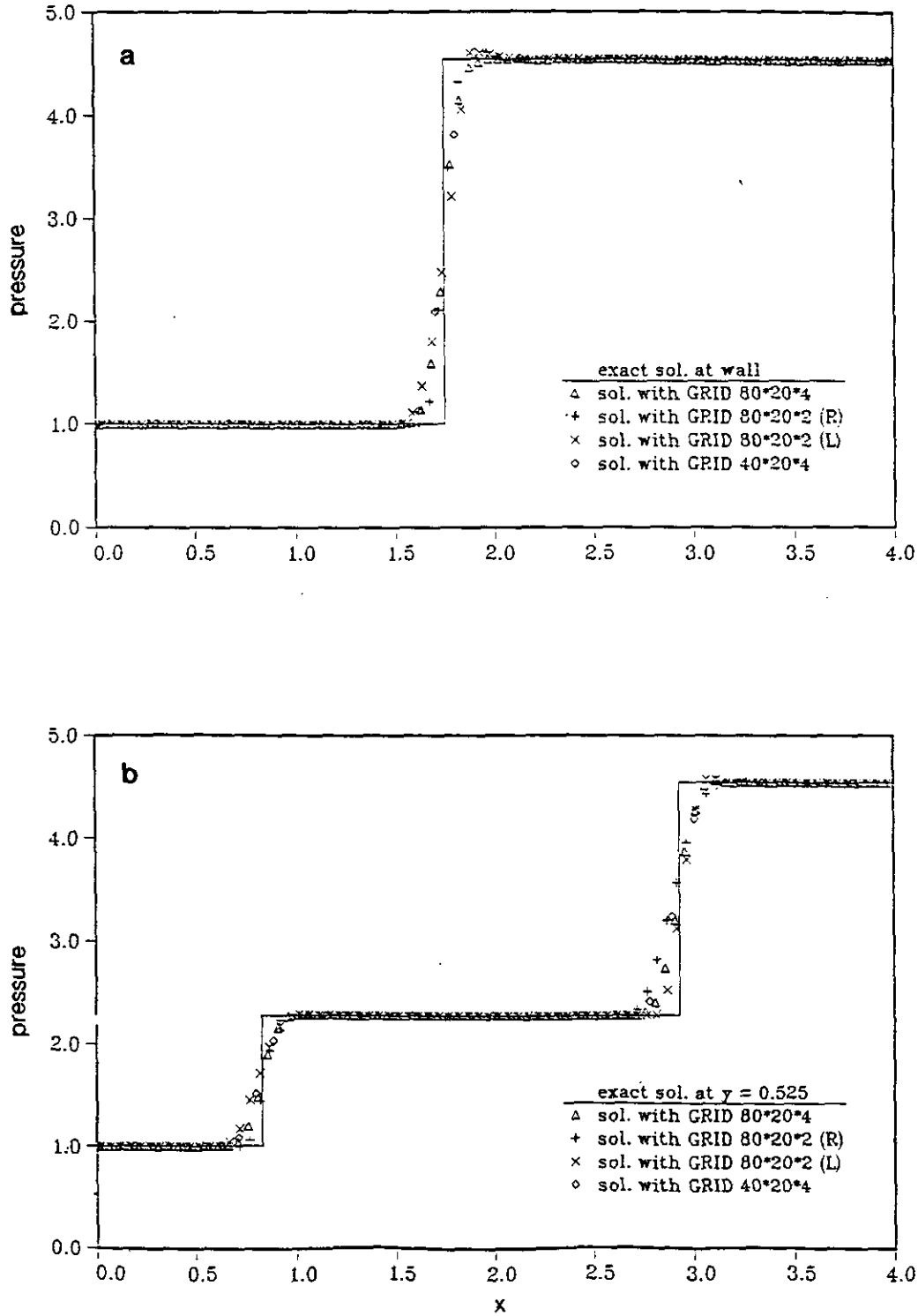

FIG. 17. (a) Pressure distribution at wall. (b) Pressure distribution at $y = 0.525$ for the oblique shock reflection problem.

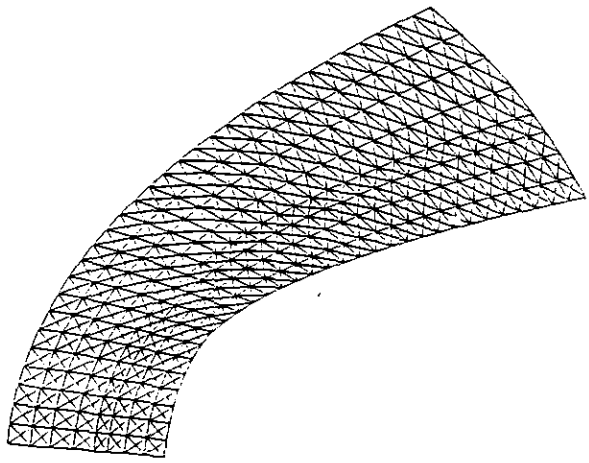

FIG. 18. The grid system $32 \times 8 \times 4$ triangles for Ringleb's problem.

TABLE VII

Errors and Order Accuracy of Density for Ringleb's Problem

$M \times N \times 4$	L_1 error	Order	L_∞ error	Order
$8 \times 2 \times 4$	3.120E−02		1.611E−01	
$16 \times 4 \times 4$	6.627E−02	2.24	3.794E−02	2.09
$24 \times 6 \times 4$	3.736E−03	1.41	2.732E−02	0.81
$32 \times 8 \times 4$	1.122E−03	4.18	6.930E−03	4.77

Note. Using the scheme with P_{ij}^3 limiter and $M = 0$.

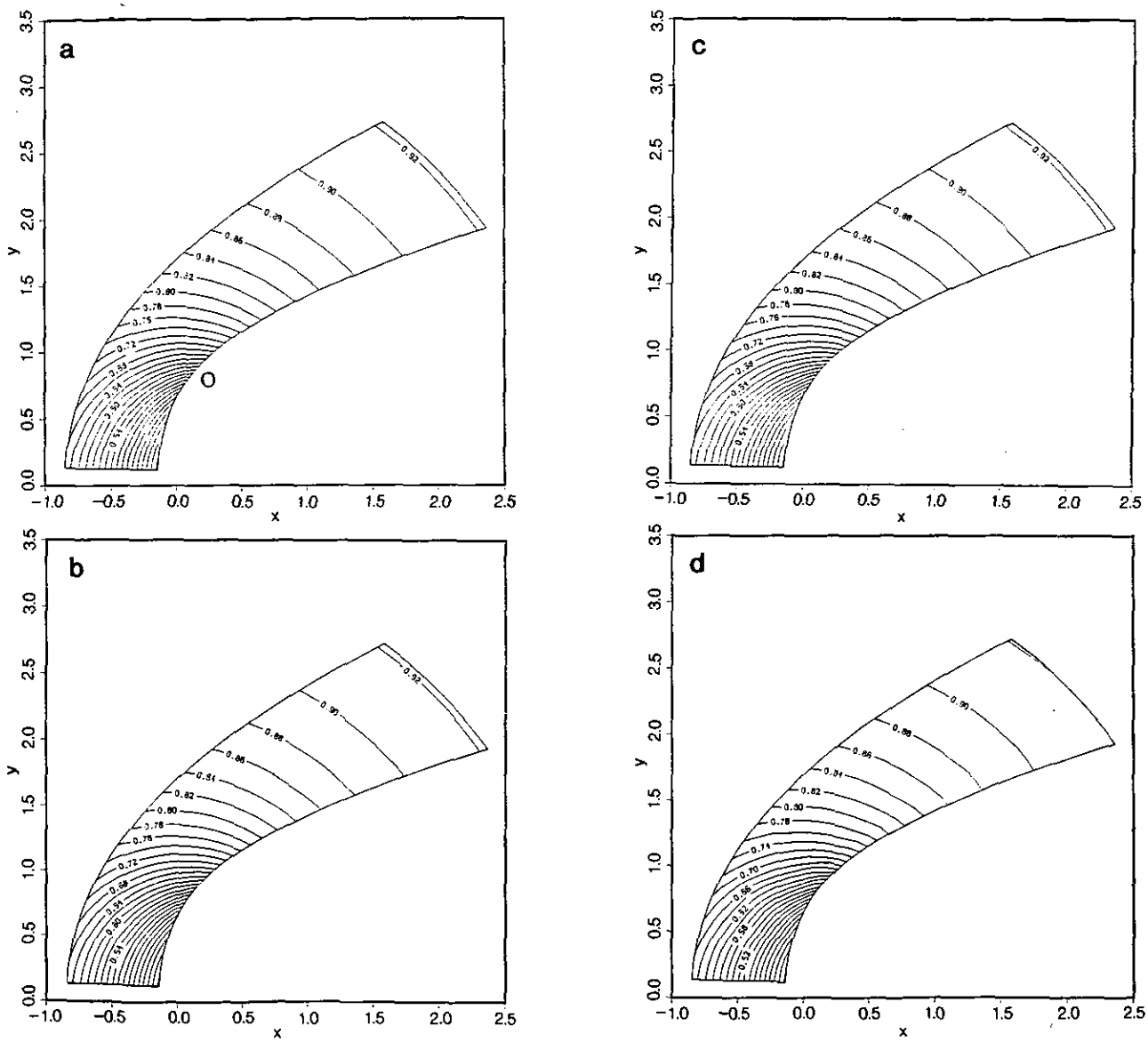

FIG. 19. The density contours for Ringleb's problem: (a) exact solution; (b) numerical solution by the scheme with no limiter; (c) with P_{ij}^3 limiter and $M = 10$; (d) with P_{ij}^3 limiter and $M = 0$.

compared two kinds of flux, Lax–Friedrichs and Godunov fluxes. The scheme with the Godunov flux is slightly better than that with the Lax–Friedrichs flux, but the scheme with the Lax–Friedrich flux seems to be accurate enough. A scheme based on TVB can dramatically improve the order of accuracy as shown in Example 5. Mesh adaptation remains to be implemented, but promises to greatly increase the power of the method as indicated in Example 4. Some smoothing methods and the treatment of boundary conditions to improve the convergence rate are the future works.

ACKNOWLEDGMENTS

We thank the referees for some constructive comments on the first version of this paper. Specifically, they pointed out the incompleteness of the proof of Theorem 2.2 and suggested that we simulate the system of equations for completeness of our work. We also express our thanks to Professor Dartzi Pan for providing a program to compute the analytic solution of Ringleb's problem and to Professor S. M. Liang for correcting our English to this paper.

REFERENCES

1. T. J. Barth and D. C. Jespersen, AIAA Paper 89-0336, Jan. 1989.
2. G. Chiocchia, *Exact Solution to Transonic and Supersonic Flows*, *AGARD*, AR-211, 1985.
3. B. Cockburn, S.-Y. Lin, and C.-W. Shu, *J. Comput. Phys.* **84**, 90 (1989).
4. B. Cockburn, S. Hou, and C.-W. Shu, *Math. Comp.* **54**, 545 (1989).
5. M. Crandall and A. Majda, *Math. Comp.* **34**, 1 (1980).
6. L. J. Durlofky, B. Engquist, and S. Osher, Triangle based adaptive stencils for the solution of hyperbolic conservation laws, *J. Comput. Phys.*, submitted.
7. A. Jameson, "Multigrid Algorithms for Compressible Flow Calculations, Multigrid Method II," in *Lecture Notes in Math., Vol. 1228*, (Springer-Verlag, Berlin/New York, 1985), p. 166.
8. S. Osher, *SIAM J. Numer. Anal.* **22**, 947 (1984).
9. P. L. Roe, *Ann. Rev. Fluid Mech.* **18**, 337 (1986).
10. C.-W. Shu and S. Osher, *J. Comput. Phys.* **77**, 439 (1988).
11. D. L. Whitaker, B. Grossman, and R. Löhner, AIAA Paper 89-0470, Jan. 1989.